Aggregation propensities of superoxide dismutase G93 hotspot mutants mirror ALS clinical phenotypes

Ashley J. Pratt[a,b], David S. Shin[a,b,1], Gregory E. Merz[c,1], Robert P. Rambo[d], W. Andrew Lancaster[e], Kevin N. Dyer[d], Peter P. Borbat[f], Farris L. Poole II[e], Michael W. W. Adams[e], Jack H. Freed[f], Brian R. Crane[c], John A. Tainer[a,b,2], and Elizabeth D. Getzoff[a,2]

[a]Department of Integrative Structural and Computational Biology and The Skaggs Institute for Chemical Biology, The Scripps Research Institute, La Jolla, CA 92037; [b]Life Sciences and [d]Physical Biosciences Divisions, Lawrence Berkeley National Laboratory, Berkeley, CA 94720; [c]Department of Chemistry and Chemical Biology and [f]Center for Advanced ESR Studies (ACERT), Department of Chemistry and Chemical Biology, Cornell University, Ithaca, NY 14853-1301; and [e]Department of Biochemistry, University of Georgia, Athens, GA 30602

Edited* by Jane S. Richardson, Duke University, Durham, NC, and approved September 19, 2014 (received for review May 21, 2013)

Protein framework alterations in heritable Cu, Zn superoxide dismutase (SOD) mutants cause misassembly and aggregation in cells affected by the motor neuron disease ALS. However, the mechanistic relationship between superoxide dismutase 1 (*SOD1*) mutations and human disease is controversial, with many hypotheses postulated for the propensity of specific SOD mutants to cause ALS. Here, we experimentally identify distinguishing attributes of ALS mutant SOD proteins that correlate with clinical severity by applying solution biophysical techniques to six ALS mutants at human SOD hotspot glycine 93. A small-angle X-ray scattering (SAXS) assay and other structural methods assessed aggregation propensity by defining the size and shape of fibrillar SOD aggregates after mild biochemical perturbations. Inductively coupled plasma MS quantified metal ion binding stoichiometry, and pulsed dipolar ESR spectroscopy evaluated the Cu^{2+} binding site and defined cross-dimer copper–copper distance distributions. Importantly, we find that copper deficiency in these mutants promotes aggregation in a manner strikingly consistent with their clinical severities. G93 mutants seem to properly incorporate metal ions under physiological conditions when assisted by the copper chaperone but release copper under destabilizing conditions more readily than the WT enzyme. Altered intradimer flexibility in ALS mutants may cause differential metal retention and promote distinct aggregation trends observed for mutant proteins in vitro and in ALS patients. Combined biophysical and structural results test and link copper retention to the framework destabilization hypothesis as a unifying general mechanism for both SOD aggregation and ALS disease progression, with implications for disease severity and therapeutic intervention strategies.

Lou Gehrig's disease | small-angle X-ray scattering | protein aggregation | protein conformation | ESR spectroscopy

ALS is a lethal degenerative disease of the human motor system (1). Opportunities for improved understanding and clinical intervention arose from the discovery that up to 23.5% of familial ALS cases and 7% of spontaneous cases are caused by mutations in the *superoxide dismutase 1* (*SOD1*) gene encoding human Cu, Zn SOD (2–4). SOD is a highly conserved (5), dimeric, antioxidant metalloenzyme that detoxifies superoxide radicals (6, 7), but overexpression of *SOD1* ALS mutants is sufficient to cause disease in mice (8). Misfolded and/or aggregated SOD species are deposited within mouse neuronal and glial inclusions (9, 10), even before symptoms appear (11, 12). Although human familial ALS has a symptomatic phenotype indistinguishable from sporadic cases (13), individual *SOD1* mutations can result in highly variable disease progression and penetrance (14, 15).

Many nongeneral mechanisms, including loss of activity or gain of function, were postulated to explain the roles of SOD mutants in ALS (3, 16–19). Recently, however, an initial hypothesis proposing that SOD manifests disease symptoms by framework destabilization (protein instability caused by structural defects) and consequent protein misassembly and aggregation has gained renewed support (2, 10, 14, 20–23). Ironically, WT SOD is an unusually stable protein (7, 24–26), and precisely how SOD mutations cause disease remains unclear. For instance, human SOD free cysteine residues C6 and C111 have been implicated in protein aggregation by promoting cross-linking (27, 28) and/or stability changes associated with oxidative modifications (29–33). Mutation of the chemically reactive thiols significantly decreases the irreversible denaturation rate for human and bovine SOD (24, 34). However, ALS mutants in a C6A/C111S SOD (AS-SOD) background (35, 36) maintain the native C57–C146 disulfide bond but can still undergo aggregation, and mutations of the free cysteines can cause ALS (37, 38). These results imply that free cysteines are not strictly required but rather, may alter aggregation kinetics (20). SOD also contains two metal ion cofactors in each subunit: a catalytic copper ion (6) and a structurally stabilizing zinc ion (34, 39, 40) (Fig. 1*A*). In higher eukaryotes, a copper chaperone for SOD (CCS) plays an important role in catalyzing both the copper incorporation and native disulfide bond formation (41). Structural analyses of apo WT SOD point to greater flexibility or increased solvent accessibility of C6 otherwise buried in the stable dimer interface (42, 43), and molecular dynamics simulations also suggest a critical role for metal ions in protein structure, because SOD's β-sheet propensity decreases in the absence of metals (44). As a result, apo SOD readily forms protein aggregates (45, 46), but the molecular structures of SOD aggregates are likely

Significance

Mutations in human Cu, Zn superoxide dismutase (SOD) cause the motor neuron disease ALS. To better understand why, we compared the aggregation, metal binding, and conformational dynamics of normal and mutant SOD proteins by using the biophysical techniques of X-ray scattering, inductively coupled plasma MS, and ESR spectroscopy. For SOD proteins with defects at a mutational hotspot, we found that copper deficiency, flexibility, and aggregation paralleled clinical severity in ALS patients. These data support a unifying protein framework destabilization mechanism for SOD-linked ALS and thereby point to potential therapies for this lethal condition with few treatment options.

Author contributions: A.J.P., D.S.S., G.E.M., R.P.R., B.R.C., J.A.T., and E.D.G. designed research; A.J.P., D.S.S., G.E.M., W.A.L., K.N.D., and P.P.B. performed research; R.P.R., P.P.B., F.L.P., M.W.W.A., and J.H.F. contributed new reagents/analytic tools; A.J.P., D.S.S., G.E.M., R.P.R., W.A.L., P.P.B., M.W.W.A., J.H.F., B.R.C., J.A.T., and E.D.G. analyzed data; and A.J.P., D.S.S., J.A.T., and E.D.G. wrote the paper.

The authors declare no conflict of interest.

*This Direct Submission article had a prearranged editor.

[1]D.S.S. and G.E.M. contributed equally to this work.

[2]To whom correspondence may be addressed. Email: jat@scripps.edu or edg@scripps.edu.

This article contains supporting information online at www.pnas.org/lookup/suppl/doi:10.1073/pnas.1308531111/-/DCSupplemental.

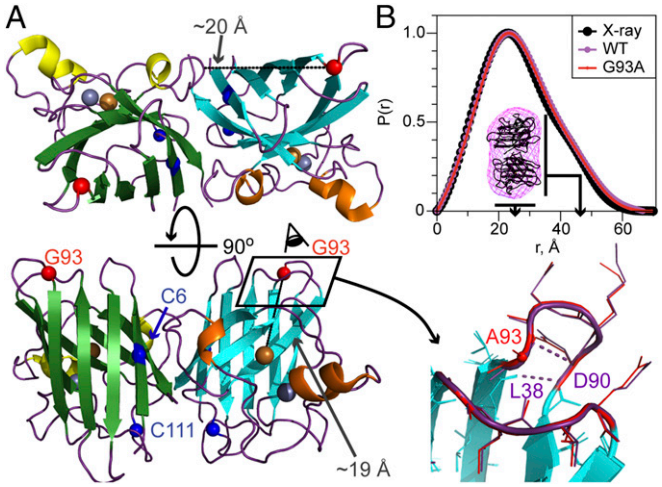

Fig. 1. Comparison of crystallographic and solution structures of WT and G93A SOD. (*A*) Overall architecture of the WT SOD dimer is displayed in 90° rotated views. G93 (small red spheres) resides on a surface-exposed interstrand loop between the fifth and sixth sequential β-strands of SOD and is expected to be innocuous in facilitating protein stability; however, this site harbors the most substitutions observed to result in ALS. G93 is also distant from both (*Upper*) the dimer interface and (*Lower Left*) the SOD active site (gold and silver spheres), which are generally implicated as the major determinants for SOD stability. Small blue spheres denote free cysteines. (*Lower Right*) The close-up view of the mutation site (boxed region in *Lower Left* tilted forward) shows high similarity between WT (purple) and G93A (red) SOD crystal structures [Protein Data Bank ID codes 1PU0 (WT) and 2ZKY (G93A)]. Hydrogen bonds characteristic of a β-bulge motif are indicated, whereby G93 (or A93) represents position 1. The main chain carbonyl group of β-barrel cork residue L38 is adjacent to the G93 site. (*B*) SAXS-derived electron pair *P*(*r*) distributions from WT (purple) and G93A (red) SOD samples in solution are compared with the theoretical curve for 1PU0. *P*(*r*) plots are normalized to peak height. Ab initio models of WT SOD derived from *P*(*r*) data are depicted in purple, with crystal structure docked into mesh envelope. Contributions to major and minor peaks from subunit and dimer dimensions are indicated.

polymorphic and represent a controversial topic (23, 47–51). The intertwined effects of the aggregation-enhancing free cysteines, dimer-stabilizing metal ions, and CCS maturation of SOD complicate the study of the ALS-causing SOD mutations themselves, and therefore, a clear cause-and-effect relationship remains obscure and requires deconvolution.

To better understand the structural effects of ALS mutations on SOD architecture, we coupled the wealth of crystallographic knowledge on SOD structure (7, 52, 53) with small-angle X-ray scattering (SAXS) experiments to characterize misassembly aggregates of ALS mutant SODs in solution. Over 20 y ago, we solved the first atomic structure of the human WT SOD protein (Fig. 1*A*) (20, 34) and proposed the framework destabilization hypothesis to explain how diverse mutations located throughout the 153-residue β-barrel enzyme might produce a similar disease phenotype (2), albeit with distinctions in the progression trajectory. Since that time, a staggering number of ALS mutations has been documented in patients [178 (mostly missense) (54)], with a similar phenotype in dogs (55, 56). Solution-based techniques are increasingly being applied to connect structure to biological outcome, for instance, through examination of intermolecular interactions within stress-activated pathways, for instance (57, 58). SAXS, which can probe structures for a wide size range of species, also provides higher resolution insights (59), for instance, over visible light-scattering techniques, readily distinguishing unfolded from folded proteins (60).

Here, we monitor the initial events of protein aggregation in a subset of ALS mutants localized to a mutational hotspot site at glycine 93. Specifically, we wished to test a possible structural basis for how G93 mutations (to A, C, D, R, S, or V) modulate age of onset and clinical severity in ALS patients (14, 15). The G93 substitution occurs in a β-bulge region (61) between sequential β-strands of the protein (Fig. 1*A*) on a protruding loop roughly ~20 Å from T54, the nearest residue of the opposing subunit, and the metal-containing active site (Fig. S1). A priori, mutation of this outer loop position would not be expected to interfere with active site chemistry or buried molecular interfaces. However, we discovered correlations of aggregation nucleation kinetics of SOD proteins with ALS mutations at this site, the stabilizing effects of metal ion retention, and available data for clinical phenotypes in patients with the same mutation. Furthermore, by measuring and exploiting the dimer geometry to observe intrinsic SOD conformers, we show that G93 mutant proteins natively reveal increased intradimer conformational flexibility in the absence of aggregation, which may reflect an increased tendency for ALS mutants to become metal-deficient and misfolding-prone and further explain the correlation to disease severity. Collective results on G93 mutants, thus, support and extend the framework destabilization hypothesis.

Results

Characterization of SOD Samples by SAXS Under Physiological Conditions. SAXS is a technique that can robustly characterize shape, size, and structure of macromolecules in solution, defining their radius of gyration (R_g), maximum dimension (D_{max}), and estimates of volume and flexibility (60). We used SAXS to establish a platform for efficiently classifying SOD samples in solution by first focusing on distinguishing WT from G93A mutant SOD. In PBS solution, these proteins are structurally similar, mirroring comparisons of their respective crystallographic structures (Fig. 1 and Fig. S2). Experimental SAXS data for proteins in solution match simulated SAXS profiles for the WT crystallographic dimer structure well, which was indicated by low χ^2 values of 1.1 and 1.2 for WT and G93A, respectively (Fig. S2). The samples have comparable R_g values (20.8 and 20.9 Å for WT and G93A SOD, respectively) and similar maximal dimensions (D_{max}; 66.5 Å and 69.5 Å for WT and G93A SOD, respectively). Subtle feature differences are noted in the *P*(*r*) electron pair distribution functions; however, overall, the real-space distributions are similar, and the crystallographic dimer is readily accommodated within ab initio electron density models calculated from the scattering data in native-like conditions (Fig. 1*B*).

SAXS-Based Assay Defines Aggregation Status of ALS Mutant SOD Proteins. In previous light-scattering and EM studies, we characterized defects in ALS mutant SODs, including the most clinically aggressive mutation A4V, in the AS-SOD background lacking free cysteines (20) by using acidic buffer conditions (pH 3.5), metal chelation (1 mM EDTA), and heat (37 °C) to induce formation of aggregated species. To further test and extend these experiments to native free cysteine containing ALS mutant SODs, we used high-throughput SAXS experiments (62) to compare G93A SOD in the true WT background with WT SOD (Fig. S3). Both WT and G93A SOD readily formed large aggregates after a 2-d incubation period, which was indicated by the turbidity of the solutions formed as well as the steep downward slopes at low scattering angle (q) in the resultant SAXS profiles. However, at shorter incubation times, differences in the extent of aggregation were apparent (Fig. S3, middle curves), suggesting differential aggregation kinetics. Furthermore, the aggregation propensity of G93A was intermediate between that of two controls, WT and A4V SOD, consistent with the clinical severity of the disease resulting from the two mutations.

To capture SOD species formed during the aggregation process, we conducted similar experiments under milder, more physiological conditions than used previously for mutants in the AS-SOD

background (20). We incubated WT and G93A SOD at neutral pH in PBS containing 10 mM EDTA at 37 °C and recorded SAXS observations for time periods ranging from 5 to 30 h (Fig. 2). From the low q scattering data, we observed substantial differences in the aggregation kinetics for these samples, which were exemplified by decreased linearity in Guinier plots for G93A relative to WT (Figs. 2 and 3, *Top Right*). For instance, after 30 h of incubation, the scattering decay is markedly different in the low q region from that of G93A, which is proportional to $\sim 1/q$, and characteristic of rod-like particles as seen for assemblies of XRCC4 with XRCC4-like factor (63). A modified Guinier plot (of $I \times q$ vs. q^2) commonly used to estimate R_c (the cross-sectional R_g of rod-like particles) also clearly exhibits linearity (Fig. 3, *Middle Right*) and increased rod length for the mutant, denoted by a downturn at lower q range (64). Furthermore, a plateau is absent in the Porod plot for G93A, indicating flexibility for the mutant under these conditions (Fig. 3, *Bottom Right*). Whereas WT SOD displays an $\sim 1/q^4$ scattering dependency in this region, indicative of a well-folded, compact particle, the Porod exponent of G93A is three, suggesting decreased compaction or increased flexibility (65). Finally, the distance distribution $P(r)$ plot (Fig. 3, *Left Inset*) reveals that EDTA treatment results in a markedly increased length (D_{max}) for the G93A aggregates. These observations and measurements are mirrored by electron micrographs of G93A SOD aggregates (Fig. S4*C*).

In Vitro Aggregation Propensities of G93 ALS Mutant SODs Mirror Clinical Phenotypes. Having established robust, yet mild, conditions for inducing SOD aggregation, we sought to characterize a larger set of ALS mutants at the G93 hotspot site. We chose the G93 site for four major reasons. (*1*) Six heritable mutations occur at glycine 93, and each seems to manifest with a distinct clinical phenotype (14, 15), with G93A (~2–3 y between diagnosis and death) followed by G93V being the most aggressive, G93S C and D being the least severe, and G93R being more variable. (*2*) By targeting a single site, we circumvent the need to deconvolute results on the basis of the mutational position and structural context (i.e., rationalizing comparisons of dimer interface, metal binding, and/or surface amino acids). (*3*) The G93A mutant SOD is one of the most well-characterized and serves as the basis for some of the first ALS disease models. (*4*) The site is located far away from determinants implicated in SOD stability (Fig. 1*A* and Fig. S1), making it an ideal candidate to test the framework destabilization hypothesis compared with proteins with mutations at dimer interface or active site locations.

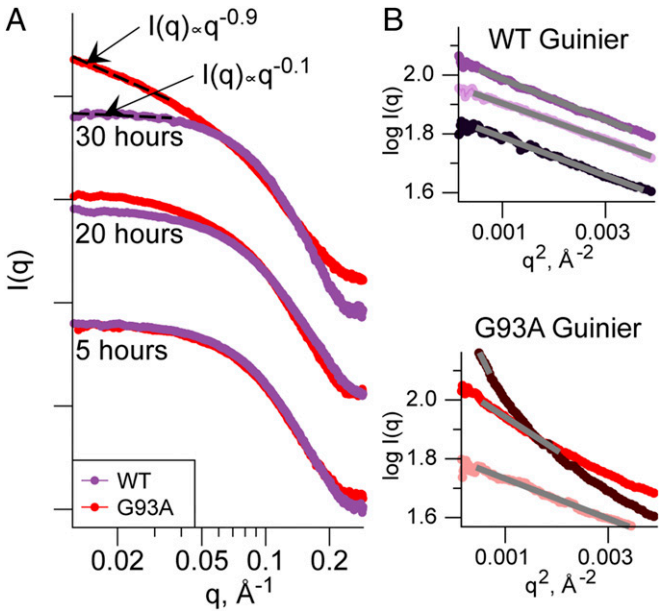

Fig. 2. SAXS monitors EDTA-induced aggregation of G93A SOD protein in solution. (*A*) SAXS profiles of WT and G93A mutant SOD at time points after incubation with 10 mM EDTA. Intensities, $I(q)$ (ordinate), are plotted in arbitrary units as a function of the scattering angle, q (abscissa). Data are plotted as a power law (log–log) plot to highlight disparities in the low q region, with successive time points offset by 1 log for clarity. (*B*) Guinier regions of (*Upper*) WT and (*Lower*) G93A further illustrate changes in aggregation behavior over time (indicated by increasing color tone). Gray lines denote linearity, such that $q \times R_g < 1.3$.

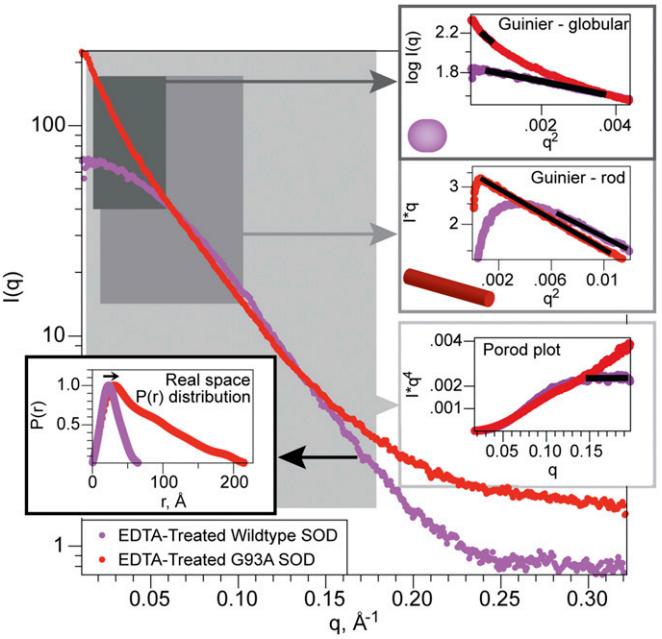

Fig. 3. Comparison of SAXS results for EDTA-treated WT and G93A SOD samples after 30-h incubation. SAXS profiles are plotted for WT (purple) and G93A (red) SOD, with the y axis as the log scale. Gray boxes denote regions of the detector intensity $I(q)$ vs. q profile subjected to additional analyses. *Top Right* and *Middle Right* are the Guinier plots for globular and rod-like particles, respectively. *Bottom Right* is a Porod plot, wherein a plateau at higher q is indicative of compact foldedness. *Left Inset* is real-space $P(r)$ distribution for WT and G93A SOD. EDTA-induced elongation of aggregate is evident for G93A but not WT SOD by comparison with Fig. 1*B*.

To identify distinctions among the G93 SOD mutant proteins in vitro, we recombinantly prepared all six G93 mutants and WT SOD and introduced them into our EDTA-based aggregation assay. Whereas no major changes in particle size were noted at 5 h of incubation after treatment with 1 or 10 mM EDTA used to initiate aggregation, striking differences in particle size became obvious after 30 h (Fig. 4 and Fig. S5). We incorporated a heat map visualization strategy (66) to comprehensively assess differences in the SAXS profiles of these species in a high-throughput manner (Fig. 4*C*). Notably, we determined that the aggregation differences seemed to correlate with the clinical severity of the mutations (Fig. 4 and Fig. S5). However, increasing size, reflected by increasing R_g values, was not proportionally accompanied by a substantial increase in the R_c during this time period (Fig. 4*B* and Fig. S5), except very slightly for larger species (note the slight sigmoidal shape in Fig. 4*B*), suggesting that all G93 mutants primarily aggregate into rods of increasing length (Figs. S4 and S6). Ab initio SAXS modeling also suggests that linear, rod-like species dominate the scattering signal. For 10 mM EDTA-treated G93A at 30 h, using a 220-Å D_{max}, a snake-shaped body is reconstructed, which is comparable

A	Rg, Å						
Patient Severity	-	varied	low	low	low	mid	high
	WT	G93R	G93C	G93S	G93D	G93V	G93A
10 mM EDTA	21.5	31.3	33.3	34.9	-	64.2	63.2
1 mM EDTA	21.2	22.4	22.3	25.2	27.5	58.4	61.3
0 mM EDTA	21.3	20.9	21.3	20.9	20.9	21.1	20.8
	Rc, Å						
	WT	G93R	G93C	G93S	G93D	G93V	G93A
10 mM EDTA	12.0	12.3	12.1	12.3	-	13.0	12.8
1 mM EDTA	12.1	12.4	12.3	12.3	12.4	12.4	12.5
0 mM EDTA	12.3	12.3	12.3	12.6	12.4	12.3	12.1

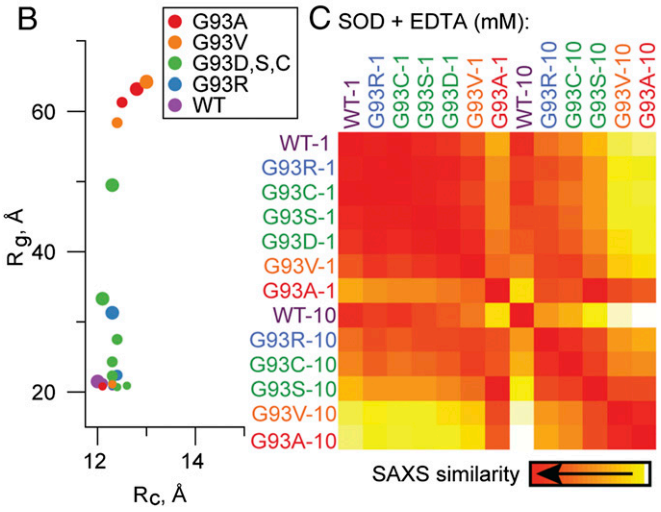

Fig. 4. Aggregate size is proportional to metal removal conditions and clinical ALS duration phenotype for G93 site mutants. (*A*) Extent of aggregation for G93 mutants treated with 0, 1, or 10 mM EDTA for 30 h is tabulated as real-space radius of gyration, R_g, which increases with the disease severity assessed from published patient mutational data, and reciprocal space R_g of the cross-section for a rod-like particle, R_c, which remains relatively constant initially in the aggregation trajectory. Mutants are grouped and color-coded by associated disease severity in patients. G93D at 10 mM EDTA was not included. (*B*) The average R_g of aggregates formed is plotted against the average R_c. Large-, medium-, and small-sized circles, color-coded as in *A*, indicate 10, 1, and 0 mM EDTA-treated samples, respectively. (*C*) SAXS profile-derived heat map globally compares 1 or 10 mM EDTA-treated (−1 or −10) samples. Red squares indicate higher overall agreement of SAXS profiles, whereas lighter colors highlight dissimilarities.

in size with an approximately four-dimer crystallographic SOD assembly with β-strands oriented perpendicular to the long axis, reminiscent of amyloid-like stacking (Fig. 5). However, aggregation reactions likely proceed by forming consecutive oligomers. Therefore, a plausible pool of species formed in solution was modeled with minimal ensemble analysis using only low-resolution information (to mitigate effects of flexibility and conformational heterogeneity) (67, 68). These results suggest a mixture of linear species of increasing length (Fig. S4*B*), which mirrors the morphology of the snake-shaped body.

Copper Protects ALS Mutants from Aggregation but Is Differentially Retained Under Acidic Conditions. To determine factors that contribute to the G93 phenotypes, we tested the impact of metal ion incorporation by analyzing the metal ion content of our samples with inductively coupled plasma MS (ICP-MS). Although all samples seemed to contain 1:1 stoichiometric levels of zinc per protein subunit, the more aggregation-prone samples copurified with lower levels of copper ion (Table S1). The copper deficiency paralleled the propensity for mutants to undergo EDTA-induced aggregation, because the size of species formed inversely correlated with the amount of bound copper at a 30-h snapshot (Fig. 6*A*).

SOD mutants often copurify with substoichiometric amounts of copper, and therefore, a common preparation strategy relies on metal reconstitution as a final purification step, which was our initial experimental approach. Given the importance of the copper deficiency to aggregation propensity, we wished to suitably distinguish copper incorporation from copper retention. We, therefore, tested whether the inability of the ALS mutants to copurify with sufficient copper was because of their inability to incorporate or retain copper, because experiments have shown that, without proper chaperones, the appropriate metal ions may not always be incorporated into their respective positions (69, 70).

To test the impact of the chaperone on copper incorporation, we implemented a purification protocol capitalizing on the coexpression of SOD with the yeast CCS homolog (71). After this procedure, we measured copper content with ICP-MS for three mutants that represent a range of clinical severity and the aggregation kinetics depicted in Fig. 4 (least aggressive: G93R, moderately aggressive: G93D, most aggressive: G93A) prepared in the CCS system. We found improved copper incorporation, comparable with that of WT SOD (~70–80%), for all these mutant enzymes (Table S1). To characterize the structure around the paramagnetic Cu^{2+} center, these samples were also analyzed by continuous wave ESR spectroscopy, and no significant differences from the WT were noted among these samples. Together, these results indicate that the G93 mutants are not precluded from incorporating or retaining copper under physiological conditions and have WT-like local copper environments.

In related experiments, we examined the removal of the metal ions from CCS/Cu^{2+}-loaded samples using established procedures (72). We discovered that the amount of residual metal retained by the ALS mutant proteins also seemed to correlate with the clinical severity (Table S1). The G93A mutant retained less copper (12.5%) and zinc (28.7%) than the WT enzyme (20.3% copper and 35% zinc). Thus, differences in the ability of ALS mutants to retain metals became apparent during perturbations, such as low pH dialysis to remove or reconstitute metals.

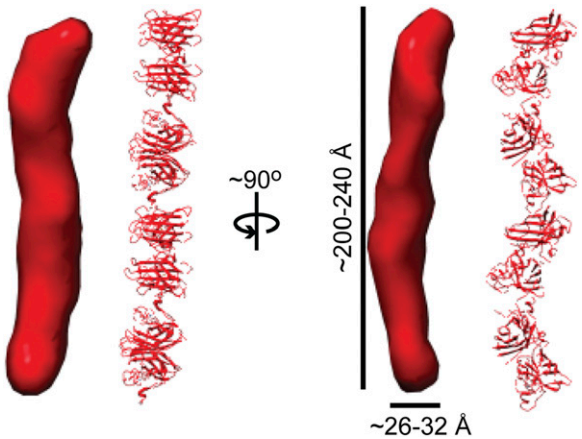

Fig. 5. Hypothetical assembly for EDTA-treated G93A aggregates. Ab initio model for a 10 mM EDTA-treated G93A sample derived from the experimental SAXS data (using a D_{max} estimate of 220 Å) suggests that the dominant species are elongated, rod-like particles (red solid) of ~1-subunit thickness. A hypothetical 8-subunit atomic model derived from the WT SOD crystal structure (Protein Data Bank ID code 1PU0) includes packing elements to emphasize shape and size similarity, and it is shown next to the solid model for ease of comparison.

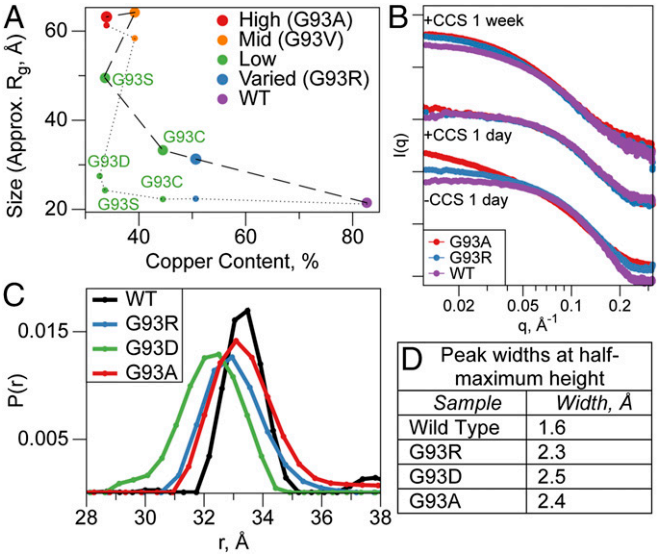

Fig. 6. Aggregation-protective effects of copper incorporation for G93 mutants and aggregation-independent conformational differences. (*A*) Extent of aggregation varies for G93 mutant SOD proteins treated with 1 (small circles) or 10 mM (large circles) EDTA for 30 h. Mutants are grouped by resulting clinical severity, which is indicated in Fig. 4. R_g is inversely proportional to copper incorporation, with dashed lines connecting samples treated with a given concentration of EDTA. (*B*) Power law (log–log) plot, where intensities (arbitrary units) are offset by 1 log for successive time points, reveals effects of cotranslational copper loading on the extent of EDTA-induced protein aggregation. Low *q* differences are notable for mutant samples prepared and expressed in the absence of CCS after 1 d of EDTA treatment (bottom plots). In contrast, extended incubation is required to induce differential aggregation for CCS-coexpressed SOD proteins, and after 1 wk, WT SOD also undergoes slight aggregation (middle vs. top plots) (Table S2). (*C*) Cu^{2+}–Cu^{2+} intradimer distances measured by pulsed dipolar ESR spectroscopy are plotted as *P*(*r*) distance distributions. Peak breadth widening appears to be associated with aggregation propensity, suggesting intrinsic conformational heterogeneity in these mutants in the absence of aggregation. (*D*) Quantification of *C* is tabulated as the peak width at half-maximal peak height.

In our EDTA-induced aggregation assay, CCS/Cu^{2+}-loaded samples failed to aggregate initially under mild conditions but exhibited modest mutation-specific aggregation after prolonged incubation (Fig. 6*B*). After a 1-wk incubation, the aggregation status of the mutants diverged from the WT sample. However, the size disparity was less drastic than for metal-reconstituted samples (Tables S2 and S3), because WT SOD is known to aggregate on prolonged perturbation (20). Dynamic light scattering (DLS) was also used to measure radii of hydration (R_h) for these samples (Table S2), revealing one predominant peak (≥99.4% mass) in the 40- to 50-Å size range for the samples and therefore, confirming the SAXS results.

To elucidate additional aspects of dimer flexibility that might explain variability associated with the G93 site, we used four-pulsed double-electron–electron resonance (DEER) experiments exploiting the paramagnetic spin of Cu^{2+} to derive Cu^{2+}–Cu^{2+} distances between adjacent subunits (Fig. 6*C* and Fig. S7). Initial experiments revealed that the relaxation time of G93A was significantly faster (~1 μs) than that of WT SOD or G93R mutants (~2–3 μs), a feature that necessitated deuteration of G93A for reproducible ESR measurements. Nevertheless, the resulting Cu^{2+} distance distributions reveal a relatively consistent peak at ~32–33 Å for all ALS mutants tested, consistent with the ~32-Å copper–copper separation in crystallographic structures. However, the breadth of the distribution was substantially wider for the mutants (Fig. 6*D*), suggesting increased dimer flexibility and/or accessibility of dynamic conformations for these ALS SOD mutants in the absence of aggregation.

Discussion

SAXS Enables Monitoring of ALS SOD Mutant Aggregation. The relationship of protein aggregation to neurodegenerative disease and the nature of the resulting aggregates are important and controversial issues. Mutant SOD proteins form aggregates within neurons and glia from ALS patients and in disease model mouse tissues, even before disease symptoms strike (10, 12, 73), but the nature of the aggregates and basis for aggregation propensity are controversial. To characterize SOD aggregation propensity in vitro, we developed an innovative SAXS-based assay and metrics to observe differences between WT SOD and G93 ALS mutants (Figs. 2, 3, 4, and 5 and Figs. S3 and S5). Of the many ALS mutants, we selected the G93 hotspot specifically because of its distal location to stabilizing factors (Fig. 1*A* and Fig. S1), the varying clinical severities among mutants, and for simplification of data interpretation. Because SOD resides predominantly in the cytosol, we incubated our samples with low concentrations of reducing agent, which eliminate complications arising from free cysteine modifications, instead of using the AS-SOD background. We also sought to avoid artifacts from harsh, nonphysiological aggregation conditions. Cellular chelators keep cytosolic metal ion concentrations low at attomolar free copper (74) and picomolar free zinc (75), which mirror the apparent binding affinities of WT SOD for copper and zinc (low attomolar and hundreds of picomolar, respectively) (76). Therefore, loss of metal ions at low to midmicromolar SOD subunit concentrations (77) would likely be irreversible, and therefore, our in vitro EDTA treatment mimics cellular metal loss. Overall, our measurements of nonaggregated SOD species test and support previous SAXS-based studies describing the overall shape of WT and ALS mutant SODs in physiological conditions (25, 78, 79), but we have extended these analyses by additionally monitoring protein aggregation changes in solution. The sizes and shapes of the species observed in our experiments are consistent with soluble, nonnative aggregates recognized by an antibody raised against misfolded ALS SOD (80). SAXS provides a robust experimental basis to assess the assembly of proteins into filaments in solution, which is seen for dsDNA break repair complexes (63). Evident from the lower and higher resolution features in our SAXS profiles, aggregation results primarily from changes in oligomerization state rather than globally aberrant folding or unfolding.

Framework Destabilization, the G93 Site, and Metal Ion Effects. The importance of the protein framework in controlling cofactor activity is a general question in biochemistry that is often difficult to examine quantitatively. WT SOD is an ultrastable protein that is sometimes purified as active protein with techniques as extreme as boiling and organic extraction (26), and the extreme specificity of packing and interactions underlying this unusual stability that controls the metal ion cofactor accessibility and activity may make the protein more susceptible to the effects of mutation (26). Furthermore, the copper ion is mobile for redox cycling during catalysis (25), and thus, the active site must be finely tuned to discriminate among substrates, intermediates, and products that differ by only a single electron. The G93 site is on the opposite end of the β-barrel from the active site, ~19 Å from the copper ion, and ~24 Å from the zinc ion (Fig. S1*A*). This mutation site is, therefore, particularly appropriate for testing of the idea that perturbation of the compact SOD framework can impact the metal ion sites, even for distant mutations. Strikingly, we do find that perturbations that decrease framework stability can, under the right circumstances, result in enhanced protein destabilization that accelerates aggregation (Fig. 7).

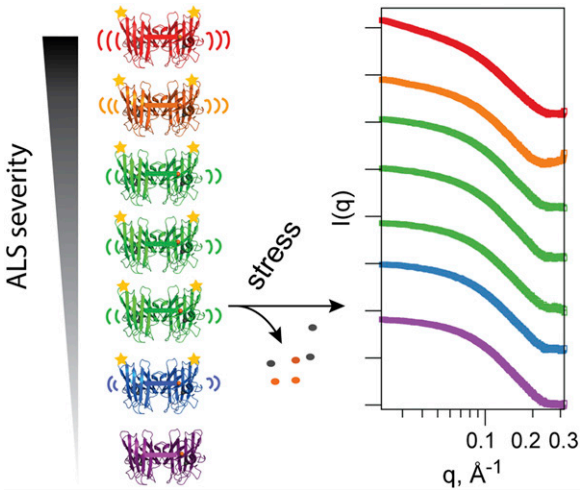

Fig. 7. Framework destabilization model for G93 mutant aggregation. (*Left*) Although G93 (gold stars) ALS SOD mutants have similar overall structures relative to WT SOD, most mutants display increased conformational flexibility (Fig. 6). This feature renders them differentially more prone to consequences from secondary events, such as metal loss (circles) on conditions of stress or dyshomeostasis (such as low pH or EDTA treatment). Over time, this can result in local unfolding or other framework and structural integrity loss features, resulting in aggregation, whereby the most aggressive mutants will display increased aggregation kinetics as exemplified by the SAXS curve schematic. This differential aggregation behavior can, in turn, manifest clinically as variable disease duration. For all of the G93 mutants examined under these conditions, the phenotype is similar, but the time course is variable. SAXS profiles are 1 mM EDTA-treated G93 mutant data from Fig. S5 plotted as a power law (log–log) plot, with *y* axis intensities (arbitrary units) offset by 1 log for each sample for clarity.

The metal ions in SOD form an integral part of its structural framework, with the Cu^{2+} ligation linking different structural elements and the Zn^{2+} ligation organizing the Zn loop (5, 39, 53). Thus, metal deficiency reduces the stability of SOD (81). Cu-free SOD has a subtly distinct structure (42, 43), and metal-deficient SOD species also have faster unfolding kinetics than the holoprotein (82). Consequently, apo SOD is capable of forming aberrant oligomers and aggregates, which are proposed to occur through a monomeric intermediate (45, 83, 84). Notably, Cu^{2+} seems more important than Zn^{2+} for kinetically stabilizing SOD (82), and for the bovine homolog, Cu^{2+} is also more important in imparting thermodynamic stability (85). Unfolding of ALS mutants seems distinct from that of WT SOD because of a preferential tendency of mutants to release copper as a first step (86), and ALS mutants retain less copper than their WT counterpart in cell culture overexpression studies (87). Furthermore, improved copper loading in ALS model mice has been associated with improved survival and locomotor function (88). These results highlight the copper site as a central, critical element energetically tied into the overall protein framework (Fig. S1*B*).

ALS mutants produced in recombinant expression systems tend to be copper- and sometimes, zinc-deficient, even with supplementation of metals in the growth media (89). Interestingly, G93 mutants with greater disease severity expressed in our chaperone-free expression system tended to copurify with less copper after dialysis with EDTA at low pH (Table S1). Some ALS mutants may have reduced binding affinities for copper and zinc (76) and may not readily remetallate (90). Nonetheless, we found that any potential reduced binding affinity for the G93 mutants could be overcome by co-overexpression of the yeast CCS. In vivo, endogenous human CCS acts enzymatically and is expressed at levels up to 30-fold lower than SOD in neurons (91), but CCS is found in protein aggregates of ALS patients (92, 93). The chaperone can also exacerbate disease phenotype in G93A-expressing transgenic mice (94), but variable effects are seen for other mutants (95). Although it is unclear whether ALS mutations lead to any aberrant CCS chemistry or interactions in vivo, genetic deletion of murine CCS in ALS model mice did not alter disease severity or progression (96). Importantly, proper incorporation of metals into ALS mutant SODs afforded by the CCS improves stability but does not preclude aggregation under adverse conditions (Fig. 6*B*).

Our ESR experiments point to distinctions between ALS mutants and WT SOD in the absence of aggregation. These differences are specific to the oxidized holoprotein and not simply the destabilized, partially metallated forms, because only Cu^{2+}–Cu^{2+} (and not Cu^{1+}–Cu^{1+}) distances are observed in the 10- to 80-Å range. Previous deuterium exchange NMR studies showed that the metal binding region of SOD exhibits increased exchange in the G93A mutant (97). We noted differences in the overall intersubunit peak breadth for several G93 mutants (Fig. 6 *C* and *D*), and related work has suggested that this feature is common to additional ALS mutants (98). Conceivably, this flexibility could enable increased conformational sampling, rendering mutant SOD proteins more susceptible to metal loss and aggregation. Therefore, our data and that of others support a model in which destabilization of ALS mutants, such as G93A, results in increased dynamics that can impact metallation and thus, assembly state.

Correlation to Disease. To bridge the enormous gap between protein structural biochemistry and human diseases, it is important to examine well-defined systems, such as a single-mutation site with differential disease outcomes, to identify potentially useful correlations. We found that ALS SOD proteins with mutations at the G93 site aggregated proportionally to both their copper deficiencies and clinical duration severities (15) (Fig. 6*A*). Although the small sample size of some genotypes (14) complicates statistical analyses and only one metric is examined here, we found similar results for A4V (Fig. S3). Correlative studies have been conducted previously. For example, in HEK293FT cells, overexpressed ALS mutants that dictate a rapid disease progression tended toward higher aggregation propensity, but mutants with low aggregation potential were suggested to be unpredictable clinically (99). However, studies of ALS mutants in the AS-SOD background failed to find correlation to disease severity (100). Others, however, found a correlation between disease duration and protein stability for noncharged apo ALS mutant SODs but noted that hydrogen bonding and electrostatics may be crucial in determining outliers (101). Stathopulos et al. (46) found that apo G93 mutants were less stable than their holo counterparts and supporting our observations, observed that the G93S and G93R mutants were the most WT-like within the set.

Combined with known SOD structural biochemistry, the collective results presented here support and extend the prediction that framework-destabilizing mutations will increase aggregation propensity. Moreover, our results argue that aggregation propensity, in many cases, will be positively correlated with ALS disease severity. The copper site provides framework-stabilizing interactions among the major protein structural elements, connecting the β-barrel to the disulfide loop (that contributes to the dimer interface) and the zinc loop (that stabilizes the subunit) (Fig. S1*B*) (5, 53). Therefore, copper ion binding promotes stability, and copper ion loss is strongly destabilizing to the native dimer assembly.

However, copper loss may not be the only result of framework destabilization. Increased conformational flexibility in ALS mutants (such as seen in our ESR experiments) could result in several secondary consequences during conditions of dyshomeostasis (including metal loss), which would, thus, dictate and promote

misfolding and aggregation in a mutant-specific fashion, leading to a similar phenotype (aggregation) but with distinct kinetics (Fig. 7). Our hypothesis, thus, also encompasses aspects of the oxidative damage hypothesis, which purports that reactive oxygen species within highly metabolic neurons put SOD at risk for oxidative damage; it was observed for hydrogen peroxide-mediated oxidative damage to active site histidine ligands, leading to copper ion release (102). Furthermore, slightly destabilized mutant proteins may be more sensitive to the effects of oxidative modification, such as glutathionylation (103), leading to their dissociation and misfolding. The destabilization hypothesis also predicts that loss of Zn (39) and ALS mutations introduced into covalently linked SOD dimers, such as those previously developed to increase serum half-life of SOD (104), would increase disease in animal models of ALS. Placing our biophysical results in the context of SOD structural biochemistry, therefore, provides the basis for a unified mechanistic hypothesis that makes specific testable predictions for disease promotion and intervention.

Summary and Perspectives. Since the framework destabilization hypothesis was proposed (2, 20), much research has, nevertheless, been aimed at testing correlations between individual or collective ALS SOD mutations and the gain of toxic functions. However, rather than pointing to distinct gain-of-function activities, these results implicate a general loss of structure-based functional stability through direct mutation-induced destabilization of the protein framework and packing or indirect destabilization through loss of copper ions for some active site mutations. Subsequent effects of structural disintegrity point to loss of copper ions, loss of zinc ions, oxidative modifications, destabilization of the dimer interface, and misassembly leading to aggregation/filamentation. This test and extension of the framework destabilization hypothesis, which specifically links destabilization of the SOD fold and assembly with decreased copper ion binding, may explain why Cu, Zn SOD destabilizing mutants promote ALS, whereas mutations of the tetrameric α-β–fold Mn SOD evidently do not (105).

With this SAXS-based assay, we were able to characterize the size and shape of ALS mutant SOD protein aggregates and collectively, link metal ion loss, flexibility, destabilization, and aggregation propensity of ALS SOD proteins with disease severity. Although our results do not prove that the pathophysiologies in ALS patients with SOD mutations are directly connected to SOD destabilization and aggregation, the correlations with clinical severity shown here are striking and support SOD protein stabilization strategies as possible disease interventions for at least a subset of patients. These discoveries and insights for a fatal neurodegenerative disease are, furthermore, relevant to elucidating the general structural biochemistry and relevance of metals in the pathophysiology underlying the many neurodegenerative diseases that involve protein aggregation propensities.

Materials and Methods

Plasmid Construction and Protein Preparation. Mutations were introduced into the SOD coding sequence using oligos from Integrated DNA Technologies and the QuikChange II Kit (Agilent). WT human Cu, Zn SOD and its ALS variants were expressed without a chaperone as described previously (20), with minor changes as described in *SI Materials and Methods*. The plasmid encoding WT SOD coexpressed with the yeast CCS was a gift from Lena Tibell (Linköping University, Linköping, Sweden), and these samples were prepared as described (71), with minor changes as provided in *SI Materials and Methods*.

Protein Analysis, Metal Analysis, and Aggregation Conditions. After purification, protein activity was verified by a gel-based assay as described (20, 106), and metal incorporation was assessed using ICP-MS as described previously (107), with minor modifications. Aggregation was induced by buffer-exchanging 2 mg/mL SOD samples into PBS with or without 1 or 10 mM EDTA (pH 8) and incubating samples and buffers for ≥24 h at 37 °C. Additional details are provided in *SI Materials and Methods*.

DLS. Thirty-microliter samples were dispensed into a 384-well, clear-bottom DLS plate and measured using a DynaPro Plate Reader DLS instrument (Wyatt Technologies). Additional details are provided in *SI Materials and Methods*.

SAXS and Graphical Analyses. SAXS experiments were carried out at the Structurally Integrated Biology for Life Sciences beamline 12.3.1 at the Advanced Light Source (62, 108). Data were collected on 15- to 20-μL samples at 2 mg/mL in PBS containing 1 mM β-mercaptoethanol or 0.25 mM Tris-(2-carboxyethyl)phosphine (with or without EDTA) at 16 °C using a MAR CCD 165 detector. Additional details are provided in *SI Materials and Methods*.

EM. G93A SOD aggregates were prepared for and imaged using negative stain transmission EM as described in *SI Materials and Methods*.

DEER. DEER experiments were carried out on a specially designed 2D-Fourier Transform ESR Spectrometer (109). Additional details are provided in *SI Materials and Methods*.

ACKNOWLEDGMENTS. We thank Jeff Speir, Sean Mulligan, Bridget Carragher, and Clint Potter for assistance with EM; Michal Hammel, Brian Chapados, and Gregory Hura for SAXS advice/expertise; Chiharu Hitomi and Camille Schwartz for technical assistance/expertise; Sunil Kumar for prior help with metal analyses; Samantha Zeitlin, Robin Gunn, John Christie, and Collin Dyer for critical reading of the manuscript; Lena Tibell for providing the CCS coexpression plasmid; and Robert Hallewell, Judith Campisi, Lisa Ellerby, Ian MacRae, and Joseph Bonaventura for insightful suggestions. SAXS data were collected at the Structurally Integrated Biology for Life Sciences beamline through the Integrated Diffraction Analysis Technologies program supported by the Department of Energy, Office of Biological and Environmental Research. ESR data were collected at the Advanced Electron Spin Resonance Technology (ACERT) National Biomedical Center. Transmission EM data were collected at the National Resource for Automated Molecular Microscopy (NRAMM), which is supported by National Institutes of Health (NIH) Grant 2P41RR017573 from the National Center for Research Resources (NCRR) and NIH Grant 9P41GM103310 from the National Institute of General Medical Sciences (NIGMS). This work was supported by NIH Grants R01GM039345 (to E.D.G. and J.A.T.) and R01GM066775 (to B.R.C.), NIH/NIGMS Grant P41GM103521 [to J.H.F. (ACERT)], and NIH/NCRR Grant P41RR016292 [to J.H.F. (ACERT)]. G.E.M. was supported by NIH Molecular Biophysics Training Grant T32GM008267. A.J.P. acknowledges the following support: the National Science Foundation Graduate Research Fellowship Program [at The Scripps Research Institute (TSRI)], predoctoral funds from The Skaggs Institute for Chemical Biology (at TSRI), and NIH/National Institute on Aging Postdoctoral Training Grant T32AG000266 in Basic Aging Research and Age-Related Disease (at Lawrence Berkeley National Laboratory) sponsored by the Buck Institute for Research on Aging.

1. Pratt AJ, Getzoff ED, Perry JJ (2012) Amyotrophic lateral sclerosis: Update and new developments. *Degener Neurol Neuromuscul Dis* 2012(2):1–14.
2. Deng HX, et al. (1993) Amyotrophic lateral sclerosis and structural defects in Cu,Zn superoxide dismutase. *Science* 261(5124):1047–1051.
3. Rosen DR, et al. (1993) Mutations in Cu/Zn superoxide dismutase gene are associated with familial amyotrophic lateral sclerosis. *Nature* 362(6415):59–62.
4. Andersen PM (2006) Amyotrophic lateral sclerosis associated with mutations in the CuZn superoxide dismutase gene. *Curr Neurol Neurosci Rep* 6(1):37–46.
5. Getzoff ED, Tainer JA, Stempien MM, Bell GI, Hallewell RA (1989) Evolution of CuZn superoxide dismutase and the Greek key beta-barrel structural motif. *Proteins* 5(4):322–336.
6. McCord JM, Fridovich I (1969) Superoxide dismutase. An enzymic function for erythrocuprein (hemocuprein). *J Biol Chem* 244(22):6049–6055.
7. Perry JJ, Shin DS, Getzoff ED, Tainer JA (2010) The structural biochemistry of the superoxide dismutases. *Biochim Biophys Acta* 1804(2):245–262.
8. Gurney ME, et al. (1994) Motor neuron degeneration in mice that express a human Cu,Zn superoxide dismutase mutation. *Science* 264(5166):1772–1775.
9. Kato S, et al. (1996) Familial amyotrophic lateral sclerosis with a two base pair deletion in superoxide dismutase 1: Gene multisystem degeneration with intracytoplasmic hyaline inclusions in astrocytes. *J Neuropathol Exp Neurol* 55(10):1089–1101.
10. Shibata N, et al. (1996) Intense superoxide dismutase-1 immunoreactivity in intracytoplasmic hyaline inclusions of familial amyotrophic lateral sclerosis with posterior column involvement. *J Neuropathol Exp Neurol* 55(4):481–490.
11. Sasaki S, et al. (2005) Ultrastructural study of aggregates in the spinal cord of transgenic mice with a G93A mutant SOD1 gene. *Acta Neuropathol* 109(3):247–255.
12. Bruijn LI, et al. (1997) ALS-linked SOD1 mutant G85R mediates damage to astrocytes and promotes rapidly progressive disease with SOD1-containing inclusions. *Neuron* 18(2):327–338.

13. Mulder DW, Kurland LT, Offord KP, Beard CM (1986) Familial adult motor neuron disease: Amyotrophic lateral sclerosis. *Neurology* 36(4):511–517.
14. Wang Q, Johnson JL, Agar NY, Agar JN (2008) Protein aggregation and protein instability govern familial amyotrophic lateral sclerosis patient survival. *PLoS Biol* 6(7):e170.
15. Andersen PM, et al. (2011) *European Handbook of Neurological Management*, eds Gilhus NE, Barnes MP, Brainin M (Wiley-Blackwell, Oxford), pp 283–310.
16. Beckman JS, Carson M, Smith CD, Koppenol WH (1993) ALS, SOD and peroxynitrite. *Nature* 364(6438):584.
17. Wiedau-Pazos M, et al. (1996) Altered reactivity of superoxide dismutase in familial amyotrophic lateral sclerosis. *Science* 271(5248):515–518.
18. Zhang H, Joseph J, Gurney M, Becker D, Kalyanaraman B (2002) Bicarbonate enhances peroxidase activity of Cu,Zn-superoxide dismutase. Role of carbonate anion radical and scavenging of carbonate anion radical by metalloporphyrin antioxidant enzyme mimetics. *J Biol Chem* 277(2):1013–1020.
19. Yim MB, et al. (1996) A gain-of-function of an amyotrophic lateral sclerosis-associated Cu,Zn-superoxide dismutase mutant: An enhancement of free radical formation due to a decrease in Km for hydrogen peroxide. *Proc Natl Acad Sci USA* 93(12): 5709–5714.
20. DiDonato M, et al. (2003) ALS mutants of human superoxide dismutase form fibrous aggregates via framework destabilization. *J Mol Biol* 332(3):601–615.
21. Johnston JA, Dalton MJ, Gurney ME, Kopito RR (2000) Formation of high molecular weight complexes of mutant Cu, Zn-superoxide dismutase in a mouse model for familial amyotrophic lateral sclerosis. *Proc Natl Acad Sci USA* 97(23):12571–12576.
22. Bruijn LI, et al. (1998) Aggregation and motor neuron toxicity of an ALS-linked SOD1 mutant independent from wild-type SOD1. *Science* 281(5384):1851–1854.
23. Stathopulos PB, et al. (2003) Cu/Zn superoxide dismutase mutants associated with amyotrophic lateral sclerosis show enhanced formation of aggregates in vitro. *Proc Natl Acad Sci USA* 100(12):7021–7026.
24. McRee DE, et al. (1990) Changes in crystallographic structure and thermostability of a Cu,Zn superoxide dismutase mutant resulting from the removal of a buried cysteine. *J Biol Chem* 265(24):14234–14241.
25. Shin DS, et al. (2009) Superoxide dismutase from the eukaryotic thermophile Alvinella pompejana: Structures, stability, mechanism, and insights into amyotrophic lateral sclerosis. *J Mol Biol* 385(5):1534–1555.
26. Shin DS, Pratt AJ, Getzoff ED, Perry JJ (2011) *Advanced Understanding of Neurodegenerative Diseases*, ed Chang RC-C (InTech, Rijeka, Croatia), pp 417–442.
27. Furukawa Y, Fu R, Deng HX, Siddique T, O'Halloran TV (2006) Disulfide cross-linked protein represents a significant fraction of ALS-associated Cu, Zn-superoxide dismutase aggregates in spinal cords of model mice. *Proc Natl Acad Sci USA* 103(18): 7148–7153.
28. Banci L, et al. (2009) Structural and dynamic aspects related to oligomerization of apo SOD1 and its mutants. *Proc Natl Acad Sci USA* 106(17):6980–6985.
29. Chen X, et al. (2012) Oxidative modification of cysteine 111 promotes disulfide bond-independent aggregation of SOD1. *Neurochem Res* 37(4):835–845.
30. Bosco DA, et al. (2010) Wild-type and mutant SOD1 share an aberrant conformation and a common pathogenic pathway in ALS. *Nat Neurosci* 13(11):1396–1403.
31. Karch CM, Borchelt DR (2008) A limited role for disulfide cross-linking in the aggregation of mutant SOD1 linked to familial amyotrophic lateral sclerosis. *J Biol Chem* 283(20):13528–13537.
32. Guareschi S, et al. (2012) An over-oxidized form of superoxide dismutase found in sporadic amyotrophic lateral sclerosis with bulbar onset shares a toxic mechanism with mutant SOD1. *Proc Natl Acad Sci USA* 109(13):5074–5079.
33. Banci L, et al. (2007) Metal-free superoxide dismutase forms soluble oligomers under physiological conditions: A possible general mechanism for familial ALS. *Proc Natl Acad Sci USA* 104(27):11263–11267.
34. Parge HE, Hallewell RA, Tainer JA (1992) Atomic structures of wild-type and thermostable mutant recombinant human Cu,Zn superoxide dismutase. *Proc Natl Acad Sci USA* 89(13):6109–6113.
35. Hallewell RA, et al. (1991) Thermostabilization of recombinant human and bovine CuZn superoxide dismutases by replacement of free cysteines. *Biochem Biophys Res Commun* 181(1):474–480.
36. Lepock JR, Frey HE, Hallewell RA (1990) Contribution of conformational stability and reversibility of unfolding to the increased thermostability of human and bovine superoxide dismutase mutated at free cysteines. *J Biol Chem* 265(35):21612–21618.
37. Nakamura A, et al. (2012) Marked intrafamilial phenotypic variation in a family with SOD1 C111Y mutation. *Amyotroph Lateral Scler* 13(5):479–486.
38. Wang Z, et al. (2014) Identification of a novel missense (C7W) mutation of SOD1 in a large familial amyotrophic lateral sclerosis pedigree. *Neurobiol Aging* 35(3):725.e11–725.e15.
39. Roberts BR, et al. (2007) Structural characterization of zinc-deficient human superoxide dismutase and implications for ALS. *J Mol Biol* 373(4):877–890.
40. Forman HJ, Fridovich I (1973) On the stability of bovine superoxide dismutase. The effects of metals. *J Biol Chem* 248(8):2645–2649.
41. Culotta VC, Yang M, O'Halloran TV (2006) Activation of superoxide dismutases: Putting the metal to the pedal. *Biochim Biophys Acta* 1763(7):747–758.
42. Banci L, Bertini I, Cantini F, D'Onofrio M, Viezzoli MS (2002) Structure and dynamics of copper-free SOD: The protein before binding copper. *Protein Sci* 11(10):2479–2492.
43. Strange RW, et al. (2003) The structure of holo and metal-deficient wild-type human Cu, Zn superoxide dismutase and its relevance to familial amyotrophic lateral sclerosis. *J Mol Biol* 328(4):877–891.
44. Strange RW, Yong CW, Smith W, Hasnain SS (2007) Molecular dynamics using atomic-resolution structure reveal structural fluctuations that may lead to polymerization of human Cu-Zn superoxide dismutase. *Proc Natl Acad Sci USA* 104(24): 10040–10044.
45. Furukawa Y, Kaneko K, Yamanaka K, O'Halloran TV, Nukina N (2008) Complete loss of post-translational modifications triggers fibrillar aggregation of SOD1 in the familial form of amyotrophic lateral sclerosis. *J Biol Chem* 283(35):24167–24176.
46. Stathopulos PB, et al. (2006) Calorimetric analysis of thermodynamic stability and aggregation for apo and holo amyotrophic lateral sclerosis-associated Gly-93 mutants of superoxide dismutase. *J Biol Chem* 281(10):6184–6193.
47. Wang J, et al. (2002) Fibrillar inclusions and motor neuron degeneration in transgenic mice expressing superoxide dismutase 1 with a disrupted copper-binding site. *Neurobiol Dis* 10(2):128–138.
48. Hwang YM, et al. (2010) Nonamyloid aggregates arising from mature copper/zinc superoxide dismutases resemble those observed in amyotrophic lateral sclerosis. *J Biol Chem* 285(53):41701–41711.
49. Kerman A, et al. (2010) Amyotrophic lateral sclerosis is a non-amyloid disease in which extensive misfolding of SOD1 is unique to the familial form. *Acta Neuropathol* 119(3):335–344.
50. Ding F, Furukawa Y, Nukina N, Dokholyan NV (2012) Local unfolding of Cu, Zn superoxide dismutase monomer determines the morphology of fibrillar aggregates. *J Mol Biol* 421(4-5):548–560.
51. Broom HR, Rumfeldt JA, Meiering EM (2014) Many roads lead to Rome? Multiple modes of Cu,Zn superoxide dismutase destabilization, misfolding and aggregation in amyotrophic lateral sclerosis. *Essays Biochem* 56(1):149–165.
52. Cardoso RMF, et al. (2002) Insights into Lou Gehrig's disease from the structure and instability of the A4V mutant of human Cu,Zn superoxide dismutase. *J Mol Biol* 324(2):247–256.
53. Tainer JA, Getzoff ED, Beem KM, Richardson JS, Richardson DC (1982) Determination and analysis of the 2 A-structure of copper, zinc superoxide dismutase. *J Mol Biol* 160(2):181–217.
54. Abel O, Powell JF, Andersen PM, Al-Chalabi A (2012) ALSoD: A user-friendly online bioinformatics tool for amyotrophic lateral sclerosis genetics. *Hum Mutat* 33(9): 1345–1351.
55. Awano T, et al. (2009) Genome-wide association analysis reveals a SOD1 mutation in canine degenerative myelopathy that resembles amyotrophic lateral sclerosis. *Proc Natl Acad Sci USA* 106(8):2794–2799.
56. Shelton GD, et al. (2012) Degenerative myelopathy associated with a missense mutation in the superoxide dismutase 1 (SOD1) gene progresses to peripheral neuropathy in Pembroke Welsh corgis and boxers. *J Neurol Sci* 318(1-2):55–64.
57. Perry JJ, Cotner-Gohara E, Ellenberger T, Tainer JA (2010) Structural dynamics in DNA damage signaling and repair. *Curr Opin Struct Biol* 20(3):283–294.
58. Rambo RP, Tainer JA (2010) Bridging the solution divide: Comprehensive structural analyses of dynamic RNA, DNA, and protein assemblies by small-angle X-ray scattering. *Curr Opin Struct Biol* 20(1):128–137.
59. Rambo RP, Tainer JA (2013) Super-resolution in solution X-ray scattering and its applications to structural systems biology. *Annu Rev Biophys* 42:415–441.
60. Putnam CD, Hammel M, Hura GL, Tainer JA (2007) X-ray solution scattering (SAXS) combined with crystallography and computation: Defining accurate macromolecular structures, conformations and assemblies in solution. *Q Rev Biophys* 40(3):191–285.
61. Richardson JS, Getzoff ED, Richardson DC (1978) The beta bulge: A common small unit of nonrepetitive protein structure. *Proc Natl Acad Sci USA* 75(6):2574–2578.
62. Hura GL, et al. (2009) Robust, high-throughput solution structural analyses by small angle X-ray scattering (SAXS). *Nat Methods* 6(8):606–612.
63. Hammel M, et al. (2011) XRCC4 protein interactions with XRCC4-like factor (XLF) create an extended grooved scaffold for DNA ligation and double strand break repair. *J Biol Chem* 286(37):32638–32650.
64. Jeffries CM, Whitten AE, Harris SP, Trewhella J (2008) Small-angle X-ray scattering reveals the N-terminal domain organization of cardiac myosin binding protein C. *J Mol Biol* 377(4):1186–1199.
65. Rambo RP, Tainer JA (2011) Characterizing flexible and intrinsically unstructured biological macromolecules by SAS using the Porod-Debye law. *Biopolymers* 95(8): 559–571.
66. Hura GL, et al. (2013) Comprehensive macromolecular conformations mapped by quantitative SAXS analyses. *Nat Methods* 10(6):453–454.
67. Pelikan M, Hura GL, Hammel M (2009) Structure and flexibility within proteins as identified through small angle X-ray scattering. *Gen Physiol Biophys* 28(2):174–189.
68. Schneidman-Duhovny D, Hammel M, Sali A (2010) FoXS: A web server for rapid computation and fitting of SAXS profiles. *Nucleic Acids Res* 38(web server issue): W540–W544.
69. Yannone SM, Hartung S, Menon AL, Adams MW, Tainer JA (2012) Metals in biology: Defining metalloproteomes. *Curr Opin Biotechnol* 23(1):89–95.
70. Cvetkovic A, et al. (2010) Microbial metalloproteomes are largely uncharacterized. *Nature* 466(7307):779–782.
71. Ahl IM, Lindberg MJ, Tibell LA (2004) Coexpression of yeast copper chaperone (yCCS) and CuZn-superoxide dismutases in Escherichia coli yields protein with high copper contents. *Protein Expr Purif* 37(2):311–319.
72. Lyons TJ, et al. (2000) The metal binding properties of the zinc site of yeast copper-zinc superoxide dismutase: Implications for amyotrophic lateral sclerosis. *J Biol Inorg Chem* 5(2):189–203.
73. Shibata N, et al. (1994) Cu/Zn superoxide dismutase-like immunoreactivity in Lewy body-like inclusions of sporadic amyotrophic lateral sclerosis. *Neurosci Lett* 179(1-2): 149–152.
74. Rae TD, Schmidt PJ, Pufahl RA, Culotta VC, O'Halloran TV (1999) Undetectable intracellular free copper: The requirement of a copper chaperone for superoxide dismutase. *Science* 284(5415):805–808.
75. Maret W, Krezel A (2007) Cellular zinc and redox buffering capacity of metallothionein/thionein in health and disease. *Mol Med* 13(7-8):371–375.

76. Crow JP, Sampson JB, Zhuang Y, Thompson JA, Beckman JS (1997) Decreased zinc affinity of amyotrophic lateral sclerosis-associated superoxide dismutase mutants leads to enhanced catalysis of tyrosine nitration by peroxynitrite. *J Neurochem* 69(5): 1936–1944.
77. Crapo JD, Oury T, Rabouille C, Slot JW, Chang LY (1992) Copper,zinc superoxide dismutase is primarily a cytosolic protein in human cells. *Proc Natl Acad Sci USA* 89(21):10405–10409.
78. Yong CW, et al. (2009) Assessment of long-term molecular dynamics calculations with experimental information on protein shape from X-ray scattering-SOD1 as a case study. *Chem Phys Lett* 481:112–117.
79. Hough MA, et al. (2004) Dimer destabilization in superoxide dismutase may result in disease-causing properties: Structures of motor neuron disease mutants. *Proc Natl Acad Sci USA* 101(16):5976–5981.
80. Redler RL, Fee L, Fay JM, Caplow M, Dokholyan NV (2014) Non-native soluble oligomers of Cu/Zn superoxide dismutase (SOD1) contain a conformational epitope linked to cytotoxicity in amyotrophic lateral sclerosis (ALS). *Biochemistry* 53(14): 2423–2432.
81. Rodriguez JA, et al. (2002) Familial amyotrophic lateral sclerosis-associated mutations decrease the thermal stability of distinctly metallated species of human copper/zinc superoxide dismutase. *J Biol Chem* 277(18):15932–15937.
82. Lynch SM, Colón W (2006) Dominant role of copper in the kinetic stability of Cu/Zn superoxide dismutase. *Biochem Biophys Res Commun* 340(2):457–461.
83. Chattopadhyay M, et al. (2008) Initiation and elongation in fibrillation of ALS-linked superoxide dismutase. *Proc Natl Acad Sci USA* 105(48):18663–18668.
84. Teilum K, et al. (2009) Transient structural distortion of metal-free Cu/Zn superoxide dismutase triggers aberrant oligomerization. *Proc Natl Acad Sci USA* 106(43): 18273–18278.
85. Lepock JR, Arnold LD, Torrie BH, Andrews B, Kruuv J (1985) Structural analyses of various Cu2+, Zn2+-superoxide dismutases by differential scanning calorimetry and Raman spectroscopy. *Arch Biochem Biophys* 241(1):243–251.
86. Ip P, Mulligan VK, Chakrabartty A (2011) ALS-causing SOD1 mutations promote production of copper-deficient misfolded species. *J Mol Biol* 409(5):839–852.
87. Bourassa MW, Brown HH, Borchelt DR, Vogt S, Miller LM (2014) Metal-deficient aggregates and diminished copper found in cells expressing SOD1 mutations that cause ALS. *Front Aging Neurosci* 6:110.
88. Roberts BR, et al. (2014) Oral treatment with Cu(II)(atsm) increases mutant SOD1 in vivo but protects motor neurons and improves the phenotype of a transgenic mouse model of amyotrophic lateral sclerosis. *J Neurosci* 34(23):8021–8031.
89. Hayward LJ, et al. (2002) Decreased metallation and activity in subsets of mutant superoxide dismutases associated with familial amyotrophic lateral sclerosis. *J Biol Chem* 277(18):15923–15931.
90. Goto JJ, et al. (2000) Loss of in vitro metal ion binding specificity in mutant copper-zinc superoxide dismutases associated with familial amyotrophic lateral sclerosis. *J Biol Chem* 275(2):1007–1014.
91. Rothstein JD, et al. (1999) The copper chaperone CCS is abundant in neurons and astrocytes in human and rodent brain. *J Neurochem* 72(1):422–429.
92. Watanabe M, et al. (2001) Histological evidence of protein aggregation in mutant SOD1 transgenic mice and in amyotrophic lateral sclerosis neural tissues. *Neurobiol Dis* 8(6):933–941.
93. Kato S, et al. (2001) Copper chaperone for superoxide dismutase co-aggregates with superoxide dismutase 1 (SOD1) in neuronal Lewy body-like hyaline inclusions: An immunohistochemical study on familial amyotrophic lateral sclerosis with SOD1 gene mutation. *Acta Neuropathol* 102(3):233–238.
94. Son M, et al. (2007) Overexpression of CCS in G93A-SOD1 mice leads to accelerated neurological deficits with severe mitochondrial pathology. *Proc Natl Acad Sci USA* 104(14):6072–6077.
95. Son M, Fu Q, Puttaparthi K, Matthews CM, Elliott JL (2009) Redox susceptibility of SOD1 mutants is associated with the differential response to CCS over-expression in vivo. *Neurobiol Dis* 34(1):155–162.
96. Subramaniam JR, et al. (2002) Mutant SOD1 causes motor neuron disease independent of copper chaperone-mediated copper loading. *Nat Neurosci* 5(4): 301–307.
97. Museth AK, Brorsson AC, Lundqvist M, Tibell LA, Jonsson BH (2009) The ALS-associated mutation G93A in human copper-zinc superoxide dismutase selectively destabilizes the remote metal binding region. *Biochemistry* 48(37):8817–8829.
98. Merz GE, et al. (2014) Copper-based pulsed dipolar ESR spectroscopy as a probe of protein conformation linked to disease states. *Biophys J* 107(7):1669–1674.
99. Prudencio M, Hart PJ, Borchelt DR, Andersen PM (2009) Variation in aggregation propensities among ALS-associated variants of SOD1: Correlation to human disease. *Hum Mol Genet* 18(17):3217–3226.
100. Vassall KA, et al. (2011) Decreased stability and increased formation of soluble aggregates by immature superoxide dismutase do not account for disease severity in ALS. *Proc Natl Acad Sci USA* 108(6):2210–2215.
101. Byström R, Andersen PM, Gröbner G, Oliveberg M (2010) SOD1 mutations targeting surface hydrogen bonds promote amyotrophic lateral sclerosis without reducing apo-state stability. *J Biol Chem* 285(25):19544–19552.
102. Mulligan VK, et al. (2012) Early steps in oxidation-induced SOD1 misfolding: Implications for non-amyloid protein aggregation in familial ALS. *J Mol Biol* 421(4-5): 631–652.
103. Redler RL, et al. (2011) Glutathionylation at Cys-111 induces dissociation of wild type and FALS mutant SOD1 dimers. *Biochemistry* 50(32):7057–7066.
104. Hallewell RA, et al. (1989) Genetically engineered polymers of human CuZn superoxide dismutase. Biochemistry and serum half-lives. *J Biol Chem* 264(9):5260–5268.
105. Borgstahl GE, et al. (1996) Human mitochondrial manganese superoxide dismutase polymorphic variant Ile58Thr reduces activity by destabilizing the tetrameric interface. *Biochemistry* 35(14):4287–4297.
106. Crapo JD, McCord JM, Fridovich I (1978) Preparation and assay of superoxide dismutases. *Methods Enzymol* 53:382–393.
107. Vaccaro BJ, Menon AL, Lancaster WA, Adams MWW (2009) *Current Protocols in Chemical Biology* (Wiley, New York).
108. Classen S, et al. (2013) Implementation and performance of SIBYLS: A dual endstation small-angle X-ray scattering and macromolecular crystallography beamline at the Advanced Light Source. *J Appl Cryst* 46:1–13.
109. Borbat PP, Crepeau RH, Freed JH (1997) Multifrequency two-dimensional Fourier transform ESR: An X/Ku-band spectrometer. *J Magn Reson* 127(2):155–167.

Supporting Information

Pratt et al. 10.1073/pnas.1308531111

SI Materials and Methods

Plasmid Construction and Protein Preparation. BL21 cells (Novagen) instead of $SOD^{-/-}$ *Escherichia coli* were used for protein expression, 100 mM each $CuSO_4$ and $ZnSO_4$ were substituted for $MgCl_2$ during osmotic shock, and $AmSO_4$-precipitated protein was removed with an additional centrifugation step before sample loading onto a 5-mL Phenyl-Sepharose FF (high substitution) column (GE Healthcare). Protein was dialyzed against 10 mM Tris (pH 7.5), separated on a 5-mL Q HP column (GE Healthcare) instead of a POROS HS ion exchange column, and eluted using a 0- to 250-mM NaCl gradient. Before metal reconstitution, protein samples were subjected to a final purification step in 20 mM Tris (pH 8) and 0.5 M NaCl on a Sephacryl S100 column (GE Healthcare). WT SOD and its ALS variants coexpressed with CCS were prepared as described (1), with minor changes. PMSF and EDTA were omitted from the lysis buffer, EDTA-free Complete (Roche) tablets were used, and the second ammonium sulfate step was omitted. For both methods, 1 mM β-mercaptoethanol (BME) was included in all purification steps, and final protein samples were buffer-exchanged into PBS (pH 7.4) before flash cooling and storage at 10 mg/mL at −80 °C. Apo-SOD samples were prepared by dialysis as described (2).

Protein Analysis, Metal Analysis, and Aggregation Conditions. For initial experiments, 50 mM citric acid–Na_2HPO_4 (pH 3.5), 150 mM NaCl, and 1 mM EDTA substituted for PBS/EDTA, and reactions proceeded for 0.5–48 h. For experiments <2 d, 1 mM BME was added to the reaction, whereas for extended time courses, pH-neutralized 0.25 mM Tris-(2-carboxyethyl)phosphine was used. Different A_{280} extinction coefficient values have been used in the literature to calculate SOD protein concentration [0.32 (3), 0.3375 (4), or 0.3 $mL{\cdot}mg^{-1}{\cdot}cm^{-1}$ (5)] based on the absorbance of the bound copper that contributes at 265 nm. The mutants prepared in this study displayed a wide range of metallation, with none at 100% copper incorporation, and therefore, we determined protein concentration using a consistent value of 0.365 $mL{\cdot}mg^{-1}{\cdot}cm^{-1}$ based on the protein sequence.

Protein samples in PBS with 1 mM BME were diluted to 1.3 mL in 2% (vol/vol) nitric acid, incubated at 37 °C with shaking at 250 rpm for 1.5 h, and then centrifuged. Samples and matching buffers were analyzed for copper and zinc content on an octopole-based 7500ce Inductively Coupled Plasma Mass Spectrometer using a MicroMist Nebulizer (Agilent Technologies).

DLS. Ten measurements were recorded for each sample, and the raw data were analyzed by using the Dynamics 7.1.7 software package with a regularization model to derive the radii of hydration.

SAXS and Graphical Analyses. The X-ray wavelength (λ) was 1.03 Å with a sample-to-detector distance of 1.5 m, and the beam size at the sample was 5.0 × 0.5 mm (6). The scattering vector q ($q = 4\pi \sin\theta/\lambda$, where 2θ is the scattering angle) range was 0.01–0.32 $Å^{-1}$. X-ray exposures between 0.5 and 5 s were taken for each sample and matching buffer blank, and the scattering of the buffer was subtracted from that of the protein. Datasets were merged with PRIMUS (7). Comparable profiles were observed for SOD samples from 2.5 to 10 mg/mL under physiological conditions, and samples of 2 mg/mL were used for aggregation experiments. The $P(r)$ function, R_g (real-space approximation), and maximum distance D_{max} were calculated with GNOM (8). Ten independent ab initio modeling jobs for WT SOD were performed using DAMMIN (9) (P2 symmetry) and averaged using DAMAVER (10). The best and worst models had χ^2 values of 1.65 and 1.73, respectively, and the average normalized spatial discrepancy was 0.65 ± 0.06. For aggregated G93A data, modeling was performed as above but using DAMMIF (11), and the best and worst χ^2 values were 1.17 and 1.23, respectively, with a model discrepancy of 0.73 ± 0.02. FOXS (12) was used for theoretical profile computation and data fitting. PyMOL (Schrodinger, LLC) and Chimera (13) were used for molecular rendering.

EM. G93A at ∼2 mg/mL was incubated in PBS containing 1 mM BME with 10 mM EDTA for 2.5 d and then diluted 1:100 in water. Three microliters were then placed on a copper–membrane–carbon grid that was plasma cleaned for 10 s using an argon/O_2 mixture. The sample was incubated for 60 s followed by a single slow blot with 2% uranyl formate that left a thin layer of the stain to air dry. Images were collected on a T2 (Tecnai F20 at 200 kV) microscope using a Tietz F416 CMOS camera using a dose of 45 $e^-/Å^2$.

Pulsed ESR Spectroscopy. SOD samples at ∼100–300 μM subunit concentrations were flash frozen in PBS containing 0.5 mM BME and 30% glycerol and maintained at 10 K during experiments. Observer pulses were made at 17.30 GHz, and the pump pulse was 17.15 GHz. After baseline correction, distances were reconstructed from the raw time domain data (e.g., as for WT in Fig. S7*A*) using the Tikhonov regularization (14) followed by the Maximum Entropy Method (15). Additional methodological details are described elsewhere (16).

1. Ahl IM, Lindberg MJ, Tibell LA (2004) Coexpression of yeast copper chaperone (yCCS) and CuZn-superoxide dismutases in Escherichia coli yields protein with high copper contents. *Protein Expr Purif* 37(2):311–319.
2. Lyons TJ, et al. (2000) The metal binding properties of the zinc site of yeast copper-zinc superoxide dismutase: Implications for amyotrophic lateral sclerosis. *J Biol Inorg Chem* 5(2):189–203.
3. de Beus MD, Chung J, Colón W (2004) Modification of cysteine 111 in Cu/Zn superoxide dismutase results in altered spectroscopic and biophysical properties. *Protein Sci* 13(5):1347–1355.
4. Goto JJ, Gralla EB, Valentine JS, Cabelli DE (1998) Reactions of hydrogen peroxide with familial amyotrophic lateral sclerosis mutant human copper-zinc superoxide dismutases studied by pulse radiolysis. *J Biol Chem* 273(46):30104–30109.
5. Stenlund P, Tibell LA (1999) Chimeras of human extracellular and intracellular superoxide dismutases. Analysis of structure and function of the individual domains. *Protein Eng* 12(4):319–325.
6. Classen S, et al. (2013) Implementation and performance of SIBYLS: A dual endstation small-angle X-ray scattering and macromolecular crystallography beamline at the Advanced Light Source. *J Appl Cryst* 46:1–13.
7. Konarev PV, Volkov VV, Sokolova AV, Koch MHJ, Svergun DI (2003) PRIMUS: A Windows PC-based system for small-angle scattering data analysis. *J Appl Cryst* 36:1277–1282.
8. Semenyuk AV, Svergun DI (1991) Gnom - a program package for small-angle scattering data-processing. *J Appl Cryst* 24:537–540.
9. Svergun DI (1999) Restoring low resolution structure of biological macromolecules from solution scattering using simulated annealing. *Biophys J* 76(6):2879–86.
10. Volkov VV, Svergun DI (2003) Uniqueness of ab initio shape determination in small-angle scattering. *J Appl Cryst* 36:860–864.
11. Franke D, Svergun DI (2009) DAMMIF, a program for rapid ab-initio shape determination in small-angle scattering. *J Appl Cryst* 42:342–346.
12. Schneidman-Duhovny D, Hammel M, Sali A (2010) FoXS: A web server for rapid computation and fitting of SAXS profiles. *Nucleic Acids Res* 38(web server issue): W540–W544.
13. Pettersen EF, et al. (2004) UCSF Chimera—a visualization system for exploratory research and analysis. *J Comput Chem* 25(13):1605–1612.
14. Chiang YW, Borbat PP, Freed JH (2005) The determination of pair distance distributions by pulsed ESR using Tikhonov regularization. *J Magn Reson* 172(2): 279–295.

15. Chiang YW, Borbat PP, Freed JH (2005) Maximum entropy: A complement to Tikhonov regularization for determination of pair distance distributions by pulsed ESR. *J Magn Reson* 177(2):184–196.

16. Merz GE, et al. (2014) Copper-based pulsed dipolar ESR spectroscopy as a probe of protein conformation linked to disease states. *Biophys J* 107(7):1669–1674.

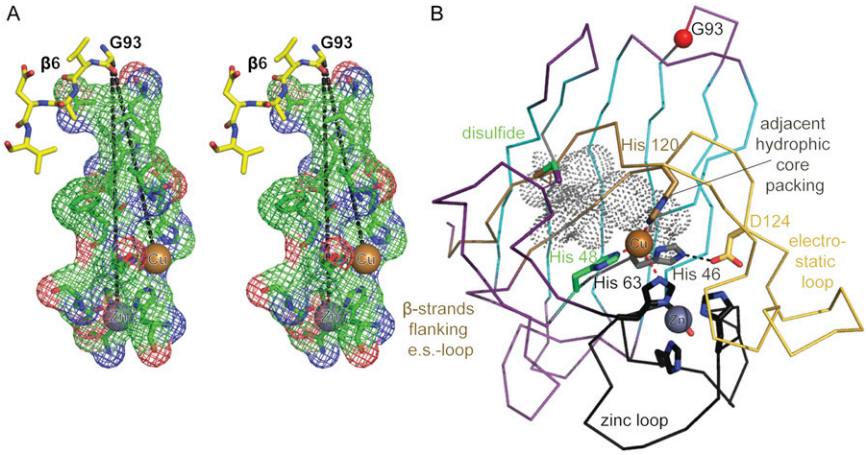

Fig. S1. Distances from key SOD structural elements to G93. (*A*) Stereo view image of G93 and the active site of one SOD subunit. The exposed G93 loop is connected to the active site metals (labeled spheres) through predictably stabilizing, dense-packing interactions (mesh) along ~19- and ~24-Å paths that transverse the β-barrel. This loop caps the β-barrel opposite the metals. (*B*) The copper site within Cu, Zn SOD is tied energetically into the β-barrel fold. All four copper histidine ligands are linked to key structural elements of the SOD framework. H46 resides adjacent to hydrophobic core residues F45, L117, and I18 (gray mesh). H48 resides near the disulfide formed between C57 and C146 (sea green). H63 forms part of the compact zinc loop (black). H120 links the electrostatic loop (yellow) to internal packing of the β-strands (two flanking strands shown in beige).

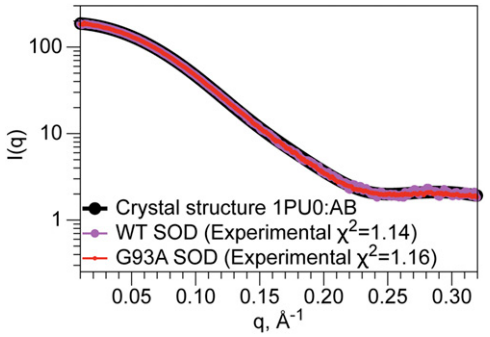

Fig. S2. SAXS profiles calculated for crystallographic WT SOD structure and measured experimentally for WT and G93A solution samples. SAXS intensity in detector units is plotted as a function of the scattering vector q ($q = 4\pi \sin\theta/\lambda$, where 2θ is the scattering angle), with the y axis plotted as log scale; the fit of the scattering data to the crystal structure (chains A and B) is indicated by χ^2 values.

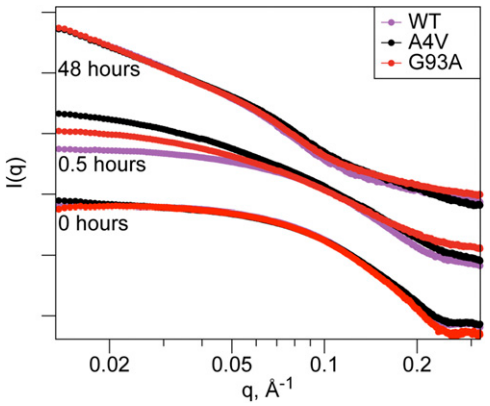

Fig. S3. Harsh treatment of WT and mutant SOD leads to production of similarly aggregated species. Combined EDTA and low pH conditions promote aggregation species for G93A, WT, and A4V control samples, although differences are noted at 0.5 h of treatment. Data are plotted as a power law (log–log) plot, with intensities (arbitrary units) from successive time points offset by 1 log for clarity.

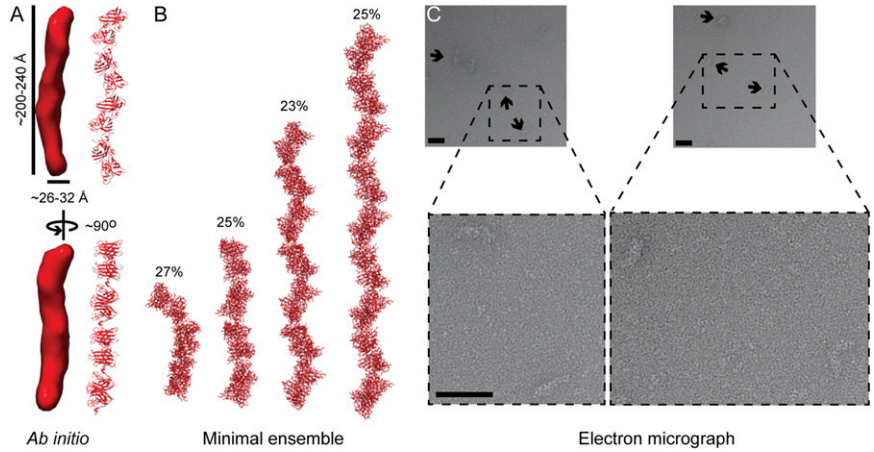

Fig. S4. Structural characterizations of metal-deficient G93A aggregates. (*A*) Ab initio modeling of 10 mM EDTA-treated G93A experimental SAXS data (1.25-d incubation with D_{max} estimate of 220 Å) suggests that signal-dominant SOD species are elongated, rod-like particles. However, these mass-averaged reconstruction models assume a homogeneous population. Assembly derived from the WT SOD structure [Protein Data Bank (PDB) ID code 1PU0] is shown next to the solid model for size-comparative purposes and fits the data with a χ^2 of 1.48. (*B*) Using a low *q* range of 0.0125–0.12, a minimal ensemble of elongated species is modeled for the same sample as in *A*. Fit of this species mixture with indicated percentages yields a χ^2 value of 0.74 (FOXS web server). Models are also based on extension of sets of dimers found within the WT SOD (PDB ID code 1PU0). (*C*) Transmission electron micrographs of 2.5-d incubated 10 mM EDTA-treated G93A aggregates stained with uranyl formate. Arrows indicate both clumpy/amorphous and elongated stained species of varying lengths. Dashed box regions are expanded below the full micrograph images. (Scale bar: 500 Å.)

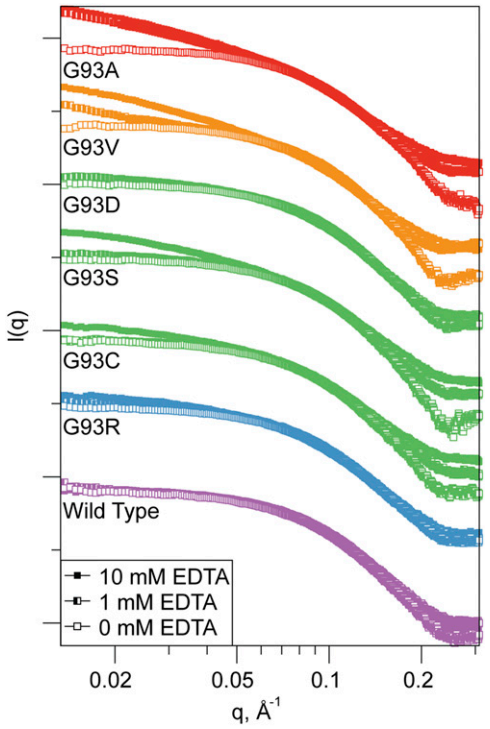

Fig. S5. Metal-chelated mutants containing free cysteines aggregate to varying extents based on EDTA concentration. WT SOD and G93 mutants treated for 30 h with 0 (empty squares), 1 (half-filled squares), or 10 mM (filled squares) were analyzed by SAXS. Data are plotted as a power law (log–log) plot, with intensities (arbitrary units) for each sample offset by 1 log for clarity.

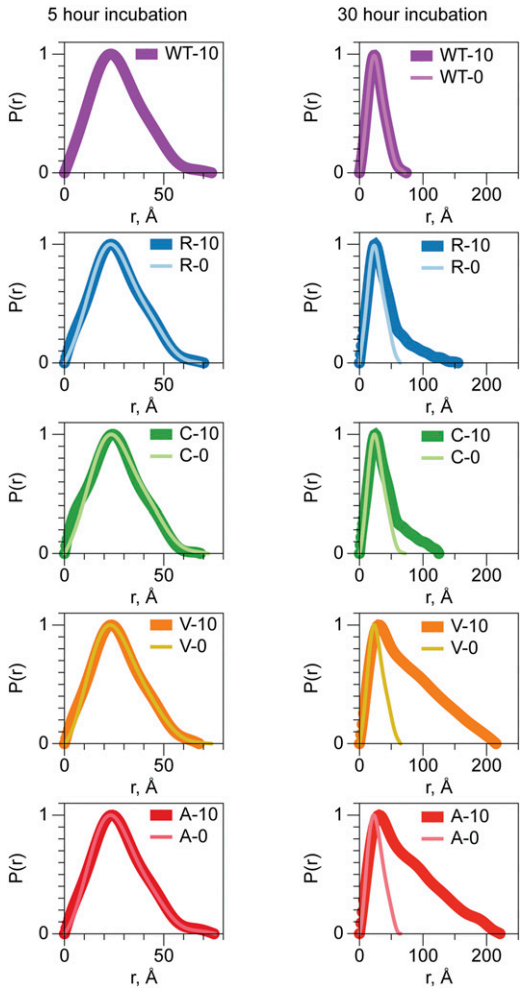

Fig. S6. Aggregation trajectory for WT and G93 mutant SODs. Real-space pairwise electron pair distributions, *P*(*r*), for selected G93 mutants representative of varying clinical severity and WT SOD reveal similarities of prenucleation species and larger aggregates. *P*(*r*) plots are normalized to peak height for ease of feature comparison. *Left* reveals data for samples incubated in 0 and 10 mM EDTA for 5 h. Note the subtle but consistent changes in *P*(*r*) features around 5, 15, and 35 Å. *Right* shows data for samples incubated in 0 and 10 mM EDTA for 30 h. Increasing propensity for aggregation of the mutants can be readily visualized by observing the D_{max} [where the *P*(*r*) curves intersect the abscissa] as a function of time in stress conditions. Note the similar changes in *P*(*r*) features around 45–50 Å with extended growth of all aggregates. Although data were not collected for the WT sample for the 0-mM EDTA 5-h incubation time point, WT SOD remained relatively unchanged after the 30-h incubation, irrespective of EDTA concentration. Similarly, *P*(*r*) plots for the WT samples incubated in 10 mM EDTA remained relatively unchanged between the two time points.

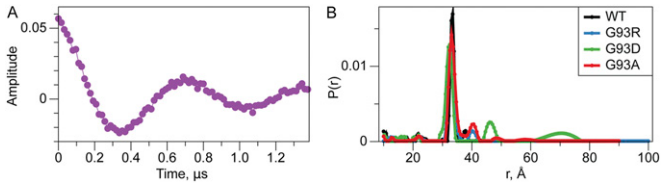

Fig. S7. Pulsed dipolar ESR spectroscopy data. (*A*) Representative raw time domain signal from WT SOD. (*B*) Full range of distance distribution data from Fig. 6*C*. Minor large-distance peaks are of unknown origin but may be artifacts of the distance reconstruction.

Table S1. Metal incorporation of recombinant SOD samples used in this work

Sample	Protein (μM)	Cu (μM)*	Zn (μM)*	Cu (%)	Zn (%)
Remetallated samples without CCS					
WT	6.4	5.3	11.2	82.6	175.7
WT-2[†]	222.0	132.0	258.1	59.5	116.2
G93A	9.4	3.2	10.9	33.9	116.4
G93A-2	6.1	1.7 (±0.1)	5.4 (±0.6)	26.7	82.8
G93C	9.1	4.1	6.7	44.5	73.2
G93D	4.3	1.4	5.3	32.7	122.2
G93R	11.4	5.8	14.4	50.6	126.4
G93S	11.1	3.7	9.4	33.7	84.9
G93V	7.2	2.8	8.1	39.2	112.3
Samples coexpressed with CCS					
WT	12.5	9.2 (±0.2)	9.3 (±0.5)	73.8	74.2
WT-2	12.5	9.3 (±1.0)	12.4 (±2.2)	74.2	99.1
WT-3	12.5	8.7 (±0.4)	12.8 (±1.3)	69.9	102.6
G93A	12.5	9.5 (±0.1)	9.1 (±0.3)	76.0	79.2
G93A-2	12.5	11.0 (±0.1)	13.8 (±0.7)	88.2	110.3
G93A-3	12.5	9.4 (±0.6)	13.1 (±1.3)	74.8	105.1
G93D	12.5	9.7 (±0.5)	6.2 (±0.4)	77.4	49.4
G93D-2	12.5	9.4 (±1.0)	13.3 (±1.6)	75.4	106.4
G93R	12.5	9.5 (±0.2)	10.0 (±0.2)	75.7	79.8
G93R-2	12.5	10.2 (±0.4)	8.8 (±0.6)	81.6	70.0
G93R-3	12.5	8.8 (±1.3)	12.3 (±1.7)	70.0	98.4
Samples treated for metal removal					
WT	12.5	2.5 (±0.1)	4.4 (±0.4)	20.3	35.1
G93A	12.5	1.6 (±0.2)	3.6 (±0.9)	12.5	28.7
G93D	12.5	1.9 (±0.1)	4.1 (±0.4)	14.9	32.4
G93R	12.5	2.0 (±0.2)	4.5 (±1.0)	16.2	35.8

Samples were analyzed by ICP-MS.

*Copper and zinc values are reported as the mean of two to three measurements of buffer-subtracted sample ± SD where applicable.

[†]No buffer was available for background correction of this sample.

Table S2. Sizes of SOD samples coexpressed with CCS and treated with 10 mM EDTA for 1 wk

1 wk + CCS	WT	G93R	G93A
R_g, Å	38.3	45.1	45.7
R_h, Å (% mass)*	41.7	47.4	49.9
R_c, Å	14.6	16.4	16.3

*DLS radius of hydration from major peak (≥99.4% by mass) determined by peak intensity.

Table S3. SAXS parameters derived from ALS mutants

Mutant	Expression	[EDTA], mM	Incubation, h	R_g, Å (Guinier)*	R_g, Å (real)	D_{max}, Å	R_c, Å†
WT	−CCS	0	0	20.8	20.9	66.5	N.D.
WT	−CCS	1	0	20.6	20.8	72.3	N.D.
WT	−CCS	10	0	20.5	20.7	72.9	N.D.
WT	−CCS	10	5	20.8	21.4	74.1	12.1
WT	−CCS	0	20	21.3	22	71.7	11.8
WT	−CCS	10	20	21.4	21.9	74.4	11.4
WT	−CCS	0	30	20.9	21.3	71.7	12.3
WT	−CCS	1	30	20.9	21.2	71.8	12.2
WT	−CCS	10	30	21.3	21.5	73.7	12
WT	+CCS	10	30	21.4	21.9	73.5	11.5
WT	+CCS	10	165	37.7	38.3	~126	13
G93A	−CCS	0	0	20.7	20.9	~70	N.D.
G93A	−CCS	1	0	20.7	20.9	70.9	N.D.
G93A	−CCS	10	0	20.6	20.8	70.9	N.D.
G93A	−CCS	0	5	20.5	21.6	76	12.5
G93A	−CCS	10	5	22	21.9	75.3	12.3
G93A	−CCS	0	20	22.7	22.2	76.6	12.3
G93A	−CCS	10	20	N.D.	27.8	~94	12.5
G93A	−CCS	0	30	21.3	20.8	67.1	12.1
G93A	−CCS	1	30	N.D.	61.3	~208	12.5
G93A	−CCS	10	30	N.D.	63.2	~221	12.8
G93A	+CCS	10	30	N.D.	25.7	~97	11.6
G93A	+CCS	10	165	N.D.	43.2	~140	16.2
G93A	+CCS	10	165	N.D.	45.7	~153	16.3
G93C	−CCS	0	5	21	21.4	72.4	12.4
G93C	−CCS	10	5	21	20.8	68.5	12.1
G93C	−CCS	0	30	21	21.3	71.6	12.3
G93C	−CCS	1	30	22.2	22.3	78.9	12.3
G93C	−CCS	10	30	N.D.	33.3	~125	12.1
G93D	−CCS	0	5	20.6	21	65.9	12.3
G93D	−CCS	10	5	20.8	21	67.6	12.4
G93D	−CCS	0	30	20.5	20.9	66.1	12.4
G93D	−CCS	1	30	N.D.	27.5	~115	12.4
G93R	−CCS	0	5	20.7	20.9	68.5	12.4
G93R	−CCS	10	5	20.7	21	70.2	12.1
G93R	−CCS	0	30	20.6	20.9	63.9	12.6
G93R	−CCS	1	30	22.6	24.3	~106	12.3
G93R	−CCS	10	30	N.D.	34.9	~155	12.3
G93R	+CCS	10	30	21.3	23	~85	12
G93R	+CCS	10	165	N.D.	45.5	~152	16.1
G93R	+CCS	10	165	N.D.	45.1	~146	16.4
G93S	−CCS	0	5	21.1	21.3	67	12.2
G93S	−CCS	10	5	20.7	21.1	70.6	12.2
G93S	−CCS	0	30	20.8	20.9	68.4	12.6
G93S	−CCS	1	30	N.D.	25.2	~99	12.3
G93S	−CCS	10	30	N.D.	49.5	~175	12.3
G93V	−CCS	0	5	20.7	21.2	74	12.5
G93V	−CCS	10	5	20.6	21.1	67.8	12.1
G93V	−CCS	0	30	21	21.1	64.7	12.3
G93V	−CCS	1	30	N.D.	58.4	~212	12.4
G93V	−CCS	10	30	N.D.	64.2	~215	13

N.D., not determined.

*$q \times R_g < 1.3$.

†$q \times R_c < 1.3$.